2D Superconductivity in $La_{2-x}Sr_xCuO_4$ Single Crystals

Gil Drachuck

2D Superconductivity in $La_{2-x}Sr_xCuO_4$ Single Crystals

Research Thesis

In Partial Fulfillment of the
Requirements for the
Degree of Master of Science in Physics

Gil Drachuck

Submitted to the Senate of the Technion - Israel Institute of Technology
Adar B 5771 HAIFA March 2011

The Research Thesis Was Done Under The Supervision of
Prof.Amit Keren
in the Faculty of Physics

Acknowledgements

I would like to thank Prof. Amit Keren for his guidance, support, patience and encouragement during my work in his group.

Special thanks to Galina Bazalizki for helping me with sample preperation and her pleasent company. I also thank Meni Shay for his help at the beginning of my work. I thank the lab technicians, Dr. Leonid Iomin and Shmuel Hoida, for their help.

Thanks to all my friends in the research group of magnetism and low tempreature for a time well spent.

Speciall thanks to Lina for her love and patience

The Generous Financial Help of the Technion is Gratefully Acknowledged

Contents

List of Figures

Abstract

We report direction dependent magnetization measurements in $La_{2-x}Sr_xCuO_4$ single crystals. The crystals were grown using traveling solvent floating zone method and were cut into rectangular needle-like shapes with the "c" direction parallel or perpendicular to the needle symmetry axis. The magnetic anisotropies were studied in details near the critical temperatures using a SQUID magnetometer. The measurements were done in the zero field limit using magnetic field $H < 1$ Oe, which was found lower than the critical field H_{c_1} at $T \to T_c$. A difference in T_c of 0.65 K was observed between parallel and perpendicular direction of the optimally doped samples (x=0.15). Higher anisotropies in T_c of 2.6 K and 4.5 K were observed in under doped samples, with x=0.08 and x=0.07 Sr doping respectively. We confirmed that the effect is not caused by sample inhomogeneity, needle dimensions, cooling rates, critical fields and vortex penetration, misalignment, etc. Although a two dimensional phase transitions is theoretically forbidden, recent theoretical and experimental efforts reported of such a phase transition in layered superconductors . Our results indicate that there is a temperature region at which $La_{2-x}Sr_xCuO_4$ exhibits two-dimensional superconductivity from a Meissner effect point of view.

Abbreviations

SC	Superconductivity
2D	Two Dimensional
AF	Anti-Ferromagnetism
SG	Spin-Glass
TSFZ	Traveling Solvent Floating Zone
LSCO	$La_{2-x}Sr_xCuO_4$
LBCO	$La_{2-x}Ba_xCuO_4$
SQUID	Superconducting Quantum Interference Device
Sr	Strontium
La	Lanthanum
Ba	Barium
Cu	Bismuth
ZF	Zero Field

Symbols

T_c	Superconducting critical temperature
H_{c1}	First superconducting critical field
ρ^s	Superfluid density
x	Strontium doping level of $La_{2-x}Sr_xCuO_4$
Δ	The superconducting gap
ΔT_c	Difference in T_c between AB and C oriented samples directions
T	Temperature
M	Magnetization
D	Demagnetization factor
J	Electric current density
A	Magnetic vector potential
H	External magnetic field
B	Total magnetic field
χ	Magnetic susceptibility
χ_m	Measured susceptibility
χ_0	Intrinsic susceptibility
$H_\perp$	Magnetic field applied perpendicular to the planes
$H_\parallel$	Magnetic field applied parallel to the planes
λ	London penetration depth
ρ_{ab}	In-plane resistivity
ρ_c	Resistivity along the c- axis
c	Speed of light

e	Electron charge

Chapter 1

Introduction

Due to the layer structure of the cuprates one might suspect that superconductivity occurs solely on the two dimensional (2D) CuO_2 planes. However, the Mermin-Wagner theorem does not allow for phase transitions in 2D. The Mermin-Wagner theorem is a general manifestation of the fact that Boss-Einstein condensation and magnetic ordering does NOT occur in 2D. Due to this theorem it was assumed that the superconducting phase transition is three dimensional, namely, there is a single T_c in which all layers become superconducting at once, with a coherent phase of the SC order parameter in all planes. The phase coherence between planes is established through the Josephson effect, whereby tunneling provides coherence even when the intervening layer is insulating. However, recent experiments show that this might not be the case. For example, J. M . Tranquada et al. [1] investigated the temperature dependence of electrical resistivity, ρ_{ab} and ρ_c, upon application of magnetic fields up to 9 T in single crystals of LBCO ($La_{2-x}Ba_xCuO_4$) with $x = 0.095$. In the configuration where H was applied perpendicular to the planes, $H_\perp$, the field had a drastic effect on ρ_c, significantly depressing the temperature at which $\rho_c \to 0$, while the effect of $H_\perp$, on ρ_{ab} was rather weak (fig. 1.1). In contrast, the effect of a parallel applied field was modest for both ρ_{ab} and ρ_c. These

results indicate that such two-dimensional phase could exist at high magnetic fields. More experimental evidence of a 2D superconducting phase were presented by Basov et al. [2] in optical reflectance measurements. A series of measurement were preformed on underdoped crystals of LSCO at a magnetic field of up to 8 T applied parallel to the crystal c-axis. These measurements revealed a complete suppression of the interplane coupling, while the in-plane superconducting properties remained intact, suggesting a 2D superconducting state.

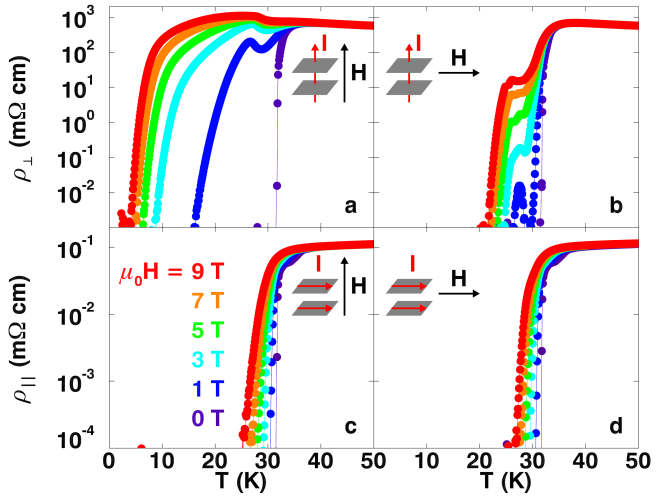

FIGURE 1.1: Magnetoresistance in LBCO with$x = 0.095$. Resisitvites vs. temperature for a range of magnetic fields with the corresponding configurations. Adapted from [3].

Two different sets of theories where devised to explain the new experiments. E. Berg and A. Kivelson proposed a theory which discuss dynamical layer decoupling in stripe-ordered, high T_c superconductors [4]. The theory argues that under certain circumstances, the superconducting condensate can occur in a two-dimensional system. This theory was proposed as the underlying cause of the decoupling of the layers as was observed by Tranquada. It was suggested that the existence of stripe order can lead to an enormous suppression of the interplane Josephson coupling, which could explains the existence of a broad temperature range in which 2D physics is apparent. Furthermore, Pekker [5] and Vojta [6], independently proposed two complementary theories with the same underlying

conclusions. Both theories discuss the different phase transitions in a weakly coupled layered system with c-axis disorder. One prediction of these theories is temperature region at which an intermediate phase exist where the in-plane superfluid stiffness, ${\rho^s}_{ab}$ (not to confuse with the resistivity), reaches a finite value while the interplane superfluid stiffness ${\rho^s}_c$ remains zero. Hence, the superfluid becomes split into and array of 2D puddles with no phase coherence along the c-axis.

However, both the Tranquada and Basov experiments were based on transport and non-DC techniques with strong applied magnetic field (9 T) which might alter the ground state properties of the system. Moreover, zero resistivity can occur along percolation paths and therefore, the true hallmark of superconductivity is the Meissner effect. In this work we examine the dimensionality of the superconducting transition using the Meissner effect in the zero field limit. We measured the magnetization of $La_{2-x}Sr_xCuO_4$ single crystals, which were cut into needles shaped samples of two different orientations, at small applied magnetic fields. By doing so, we managed to measure the clean AB-plane and the C-axis diamagnetic response. The major finding of this work was an anisotropy of the superconducting transition temperature between the two directions. All of the samples oriented with $H_\perp AB$ (perpendicular to the planes), consistently exhibited higher T_c than the $H_\parallel AB$ (parallel to the planes) samples. This phenomena was thoroughly tested, repeated for various dopings and was found to be doping dependent as well. Our results imply that at a certain temperature range, the superconducting phase transition in LSCO ($La_{2-x}Sr_xCuO_4$) is two dimensional.

1.1 The $La_{2-x}Sr_xCuO_4$ Compound

High-T_c Superconductivity in cuprates was discovered in 1986 [7]. Bednorz and Müller found that the LBCO system had a superconducting transition temperature at $T_c = 30K$. Later that year, the LSCO compound was discovered, exhibiting superconductivity up to 38 K. The record T_c was broken one year later with the discovery of the Y-Ba-Cu-O system having a transition temperature of 91 K [8]. In the following years T_c reaching up to 164 K under high pressure [9] was discovered in a mercury based cuprate. The name "Cuprates" actually arises from the key feature shared in these compounds, namely, the crystalline structure consists of layers of copper oxide planes, separated by ions of rear earth elements. The spacing between Cu ions is about 3.78 Å. Between the neighboring Cu-O planes in LSCO, there are two layers of La(Sr)-O planes. Figure 1.2 demonstrates the crystalline structure of LSCO, who has the simplest structure of the cuprates family.

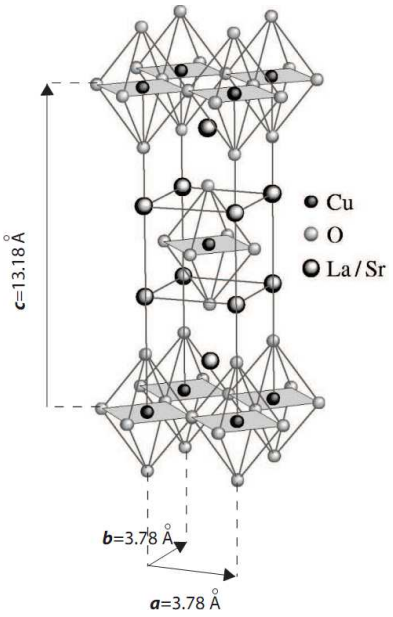

FIGURE 1.2: The crystalline structure of $La_{1-x}Sr_xCuO_4$. (adapted from [10])

In contrast to the "old" metallic superconductors, the cuprates can be doped and their charge carrier concentration can be varied. In order to understand the doping mechanism in LSCO it is sufficient to look at the charge distribution of one unit

cell. The valance of La is $^{3+}$ and of O is $^{2-}$. Therefore, in the parent compound ($x = 0$) all the Cu ions are in a Cu^{2+} state, namely, they have one unpaired electron in a d shell. As x increases, the carrier concentration in the Cu-O planes is determined by "charge reservoirs" inserted between the Cu-O planes. Since the valance of Sr is only $^{2+}$, increasing the Sr content by x attracts negative charge from the Cu-O planes while leaving holes on the Cu sites. Therefore, the hole concentration in LSCO is proportional to the Sr content in the unit cell.

The physical properties of cuprates changes drastically as the doping varies. Many phases with exotic physical properties have been discovered as the doping x and the temperature T are changed [11], though not all will be reviewed in this work. Figure 1.4 illustrates the phase diagram of hole-doped cuprates as a function of doping. As shown in fig. 1.3, in the undoped parent compound, the electron spins are arranged in an anti-ferromagnetic (AF) configuration on the Cu-O planes. Once holes are introduced into the system, the long range anti-ferromagnetic order is disrupted. The Neel temperature T_N of this phase reaches room temperature at $x = 0$ and rapidly decreases with small variation of x, until it completely vanishes at $x = 0.02$. On the other hand, high T_c superconductivity extends between $x = 0.055$ and $x = 0.26$, with the maximum transition temperature $T_c \simeq 38K$ happening around $x = 0.15$. The doping with the highest T_c is called the optimal

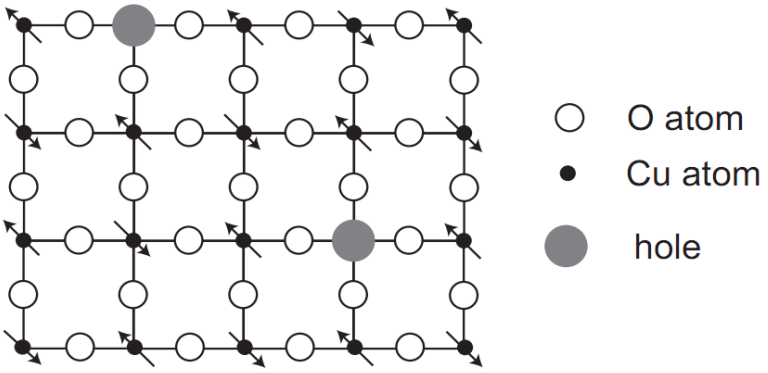

FIGURE 1.3: Schematic drawing of the Cu-O plane

doping, while the region with lower doping is called the underdoped region, and that with the higher doping is referred to as the overdoped region. Since the T_c vs. x curve form a dome-like region, the superconducting phase is often called "superconducting dome". Moreover, many experiments suggest that the the order parameter of cuprates has d-wave symmetry, i.e. $\Delta(k) = \Delta_0(\cos(k_x) - cos(k_y))$, in contrast to conventional superconductors with s-wave symmetry of the order parameter. In the region between AF and SC, $x = 0.02$ to $x = 0.05$, short range magnetic order remains in the system in a spin glass phase (SG), which coexists with superconductivity up to $x = 0.08$ [12]. Above $x = 0.27$, superconductivity vanishes and LSCO behaves as a normal metal.

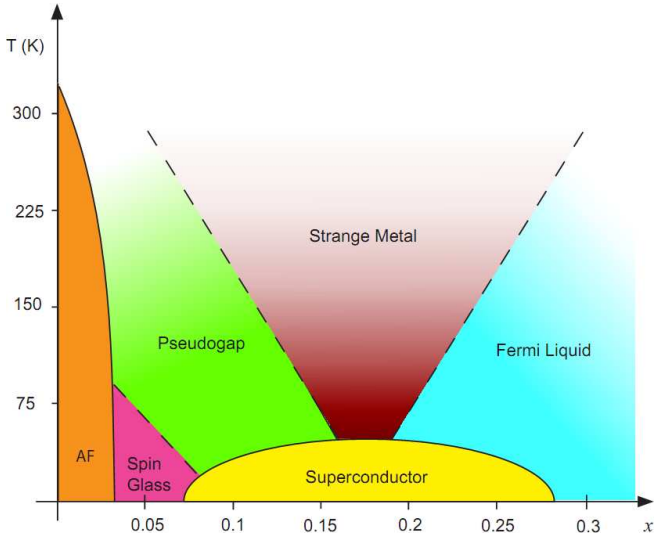

FIGURE 1.4: The phase diagram of cuprates.

Chapter 2

Experimental Methods

In this chapter we will cover the different techniques used to prepare, analyze and measure single crystals of LSCO. We begin with an introduction to crystal growth using Traveling Solvent Floating Zone Method (TSFZ), continue with the SQUID magnetometer and Laue Camera. Finally, we will describe the preparation of unique samples for this experiment.

2.1 Traveling Solvent Floating Zone Method

2.1.1 General Description

Crystal growth using the optical floating zone technique has been extensively used to grow a variety of bulk crystals, particulary of metal oxides such as cuprate superconductors. A Large high quality single crystal enables a reliable measurement of physical properties, and is specially important for studying direction dependent properties. High-T_c cuprates superconductors melt incongruently. Namely, the cuprates does not melt uniformly and decompose into other substances after solidification, hence growth methods that rely on direct crystallization from self

melt are rendered useless for the cuprates. Therefore solution growth have been developed to grow crystals of cuprates. One of the popular methods to grow the high-T_c materials is the Traveling Solvent Floating Zone Method (TSFZ), which allows a high degree of control of the crystal growth parameters.

2.1.2 The image furnace

In all image furnaces, the basic concepts is that either ellipsoidal or parabolic mirrors is used to focus light from halogen or xenon lamps onto a vertically held feed rod to produce a molten zone. Figure 2.1 presents a schematic view of the image furnace core parts. The feed and seed material rod are placed inside a quartz tube and mounted on vertical shafts that can be rotated with a variable speed in the same or opposite directions. The quartz tube is used to create a controlled atmosphere, either high pressure of Argon, Nitrogen and oxygen gas mix, or vacuum if required. The gap between the two rod is then placed at the common focal point where the temperature can be as high as 3000 ^{o} C, which depends on the sample absorption, lamp power, and the applied voltage on the lamps. The high temperature zone melts the rods and creates a molten zone between them. The molten zone is then passed trough the feed rod at desired speed, the melt then crystalizes after moving out of the high temperature zone. An example of this process is show in fig 2.2.

2.1.3 Key Process Parameters in Crystal Growth

When growing crystals with the TSFZ method the growth parameter space is very big, nonetheless there are some parameters which play a more significant role than others. Therefore, there is and order in which each parameter is optimized.

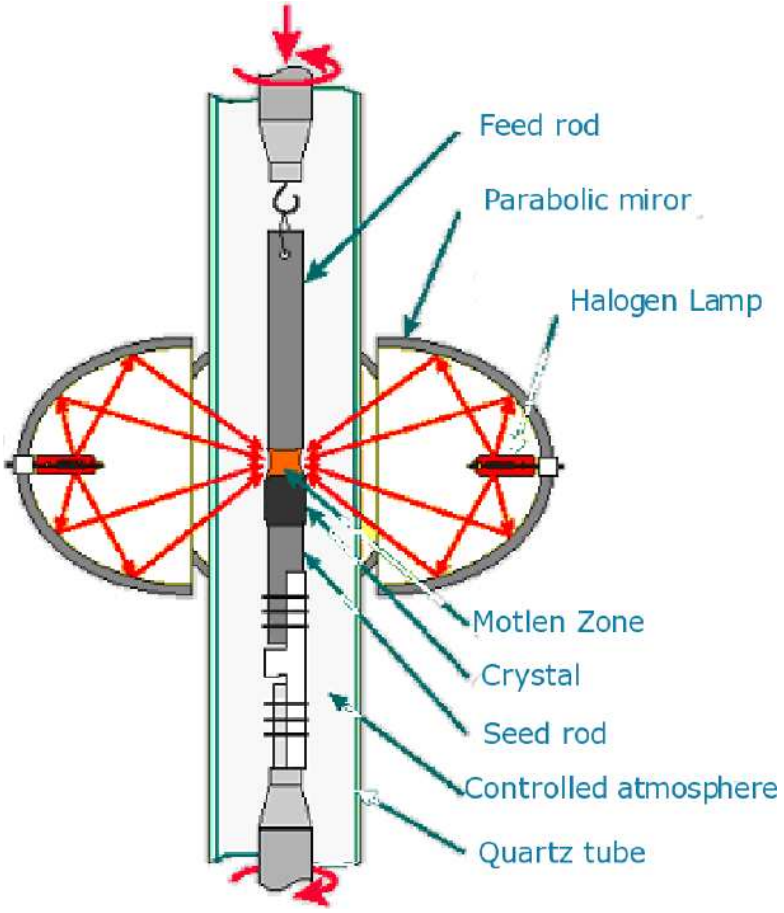

FIGURE 2.1: The inner core parts of the floating zone image furnace.

FIGURE 2.2: (LH) The floating zone furnace at work. (RH)Feed and seed rod are connected with a molten zone in between during crystal growth.

High quality feed rod

The preparation of a feed rod is the initial stage of crystal growth using the TSFZ method. For feed rods made from compacted powder, such as most metal oxides, excess porosity can undermine the stability of the molten zone due to penetration of the melt into the feed rod. This penetration can be attributed to a capillary effect in which the melt is partially absorbed by the cavities among between the fine particles in the feed rod.

For most materials, such porosity can be decreased by either increasing the pressure at which the rod is compacted or sintering the feed rod at temperatures near its melting point prior to loading it to the image furnace.

Therefore a uniform feed rod should be as close to final crystal density as possible, have a constant diameter and homogeneous composition and chemistry which is critical to achieve a stable molten zone and grow a high quality single crystal.

Crystallization rate (growth speed)

The growth speed or crystallization rate is unarguably one of the most critical parameters governing crystal quality when using the floating zone technique. Crystallization rate can strongly vary from 240 mm/h (GaAs) to 0.05 mm/h (Bi-based superconductors). It has been widely reported that changing growth speed can affect the grown crystal in terms of crystal size, formation of bubbles, cracks, chemical composition, crystal alignment, twin formation and has a great influence on the solid-liquid interface and molten zone stability. The growth rate is mainly restricted by the slow solution diffusion process at the solid-liquid interface boundary, thus the typical growth rate required for optimal crystal quality depends on

whether the materials melt congruently or incongruently. For congruently melting materials the composition of the molten zone is the same as the feed rod, crystallization process is not much limited by slow diffusion processes and relatively higher growth speed can be achieved. For incongruently melting materials the composition of the melt differs from one of the original solid, the compositional differences necessitate solution diffusion at the solid-liquid interface, which generally takes place slowly and therefore limits growth speed to a very slow rate.

Growth atmosphere and gas pressure

Both atmosphere and gas pressure are crucial parameters when growing crystal in the TSFZ method and play a key difference between success and failure. Both of these parameters are fairly easily controlled during the crystal growth by selecting the right gas mixture coming in, and the desire pressure coming out from the quartz tube. The main reason quoted for growing in higher than atmospheric pressure is to reduce the vaporization of volatile components from the sample. Reduction of evaporative losses is advantageous for growth of more stoichiometric single crystals.

Lamp power and temperature of the molten zone

The "right" power level depends mainly on the chemical properties of the grown material, but is also affected by factors such as gas content and pressure, growth rate ,density and diameter of the feed rod ,lamp de-focusing and the temperature gradient around the molten zone. For incongruently melting materials it is extremely important to adjust the power level according to the material's phase diagram, then it must be kept constant. Failing to fulfil this condition will result

in either secondary phases or completely wrong chemical composition of the grown crystal.

$La_{2-x}Sr_xCuO_4$ Crystal Growth

Powders of CuO (99.9%), La_2O_3 (99.99%) and $SrCO_3$ (99.9%) were dried at high temperature (between 500 ^oC ^{o} 1050 C), then weighted accordingly to the calculated stoichiometric values. The desired doping level of the end product crystal is therefore determined in the beginning of process by adding the right amount of $SrCO_3$ into the mixture. An extra 2.5% of CuO where added due to evaporation during the crystal growth. The weighted powders were mixed and grinned together until smooth and homogeneous texture materialized. The mixed powder was placed in alumina crucible and underwent firing at 960 ^{o} C in a box furnace. Such high temperatures induces diffusion of the reactants and binds the chemical together to form $La_{2-x}Sr_xCuO_4$. The grinding and firing process was repeated three time in order to eliminate possible impurity phases. After this process was completed, powders were inspected with x-ray analysis to ensure right doping concentration and purity. The second stage of preparation involves making a cylindrical shaped rod, which will be used as a feed and seed for the crystal. The powder mixture was compacted in to a rubber tube which was then inserted into an isostatic press. Isostatic pressure of up to 60000 psi (4000 bar) compacts the powder into a long rod (up to 20cm), reaching $d \approx 60\%$ of the crystal density. The compacted rod were sintered at $T = 1230$ ^{o}C near it's melting point temperature for 24h. This step brings its density very close ($d > 95\%$) of the crystal density. It prevents the effect of solvent being sucked up by the feed rod allowing smooth uninterrupted growth. Figure 2.3 demonstrates such feed rod.

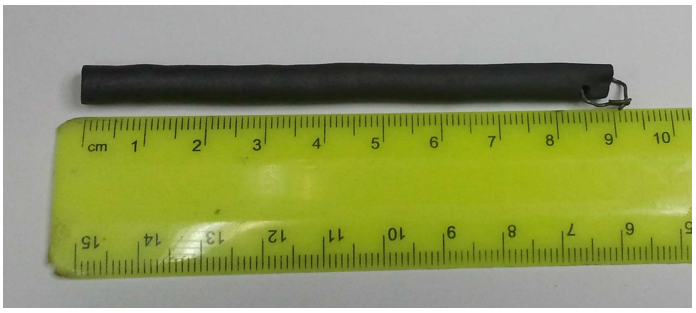

FIGURE 2.3: A sintered feed rod of LSCO.

The crystals were grown under elevated pressure of mixed Argon/Oxygen (10:1) atmosphere. A slow rate of 1 mm/hour (24 mm/day) was chosen to let the diffusion in the melt take place, the liquid and the solid being of different composition. Feed and crystal were rotated in opposite directions at 15rpm in order to improve the liquid homogeneity. All experiments were ended voluntarily after the whole feed rod was consumed by growth, yielding to black semi-metallic color crystal with lengths ranging from 70 mm to 110 mm with a typical diameter of 4 mm to 6 mm depending on the starting rod dimensions and pull rate of the feed rod. An exemplary crystal is shown in fig. 2.4. After growth, the crystal were annealed in Argon atmosphere to remove excess oxygen and relieve thermal stress.

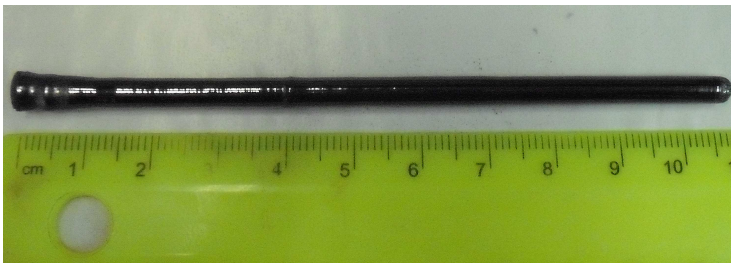

FIGURE 2.4: As grown single crystal of LSCO.

2.2 Laue Diffraction Method

The Laue method was the vehicle for the discovery of the diffraction of x rays by crystals ninety years ago. Nowadays it is mainly used to determine the orientation of large single crystals. In the Laue method, Mo x-ray radiation is allowed to

fall on a fixed crystal, and is reflected from it. The diffracted beam forms an array of spots on a plane defined by a CCD (Charged-Coupled Device) camera (fig .2.5). Each point defines an angle between the going out beam, the crystal, and incoming beam. It also defines the crystallographic planes from which the x-rays are reflected. The angle θ and the spacing between planes d fulfilling Bragg's law. A particular wavelength from the white radiation spectrum satisfies the Bragg's law (eq. 2.1), for the specific θ and d values involved.

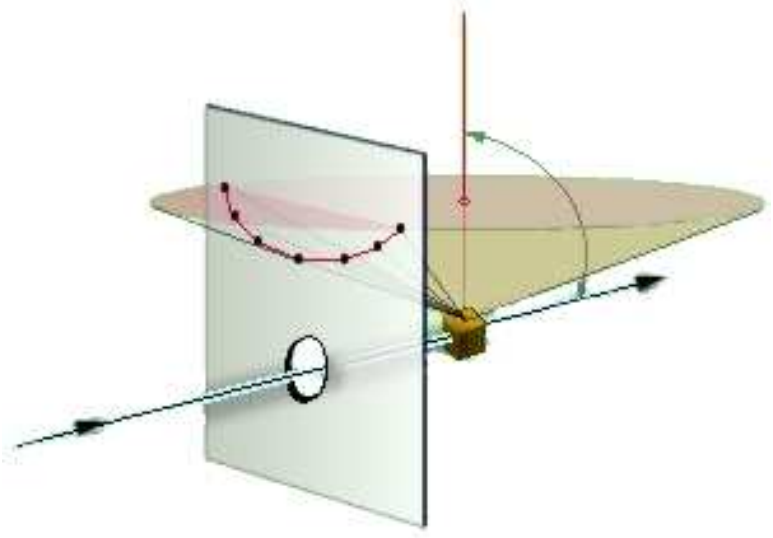

FIGURE 2.5: Illustration of the Laue method principal.

$$n\lambda = 2d\sin\theta \tag{2.1}$$

Each diffraction point corresponds to a different wavelength therefore it corresponds to a different plane. The end result is a typical laue diffraction pattern that represents the symmetries of the analyzed crystal and its orientation. The Laue images which are presented in this work were measured using Photonic Science Laue camera with an XOS source emitting wavelengths ranging from $0.35-\mathring{A}$ to $2.35\mathring{A}$. Interpretation of diffraction patterns was made possible using a software

named "Orient Express" which can simulate and fit such patterns, given the crystal structure, lattice parameters, source-detector configuration and sample geometry.

2.3 Orientation and Cutting

In this work our purpose was to measure the magnetic susceptibility (χ) of LSCO with the external magnetic field pointing in two different crystallographic directions. For this purpose needle like samples had to be cut out of the cylindrical crystal since χ depends on the sample geometry via the Demagnetization factor (D) which is further discussed in Appendix A the measured susceptibility χ_m is given by eq. 2.2:

$$\chi_m = \frac{\chi_0}{1 + D\chi_0} \tag{2.2}$$

where χ_0 is the interesting quantity. For needles like samples $D \simeq 0$ and χ_m equals χ_0. Figure 2.6 presents the chosen configuration.

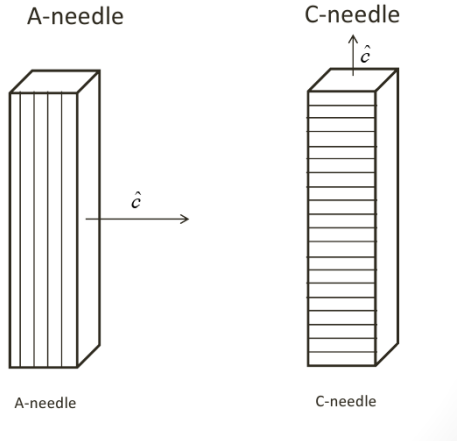

FIGURE 2.6: Illustration of the samples in the experiment. *A*-needle and *C*-Needle sample geometries were used for the measurements.

To achieve these sample requirements the crystal must be oriented to a high degree of confidence and carefully cut. This was performed in several steps with a

precision 3-axis goniometer which can move as one piece from the Laue camera to a diamond circular saw. The fact that LSCO grows with the c-axis on it's side helped tremendously to the sample preparation. *A*-needle samples were cut from 10 mm segments along the growth direction. The rod was mounted using shift-wax (made by Nikka Seiko LTD.) on the goniometer and oriented in a manner where the *C*-axis is pointing to the camera (fig. 2.7) with the saw cutting parallel to the CuO_2 planes. The result is a rectangular plate which is further cut into an *A*-needle.

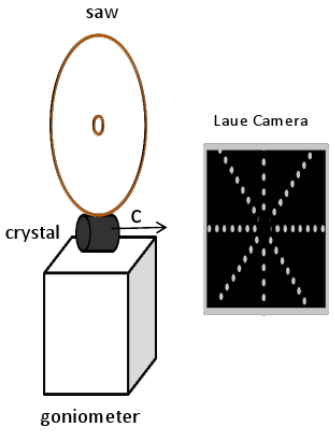

FIGURE 2.7: Illustration of the setup for cutting *A*-needle samples.

C-needle samples were cut and oriented from disks that were cut out of the rod. It was challenging to making these samples due to LSCO's (001) cleavage plane. Therefore *C*-needles had to be cut with a delicate diamond wire saw which applies no pressure on the crystal while cutting the needle. Figure 2.8 demonstrates different Laue patterns taken from different sample geometries.

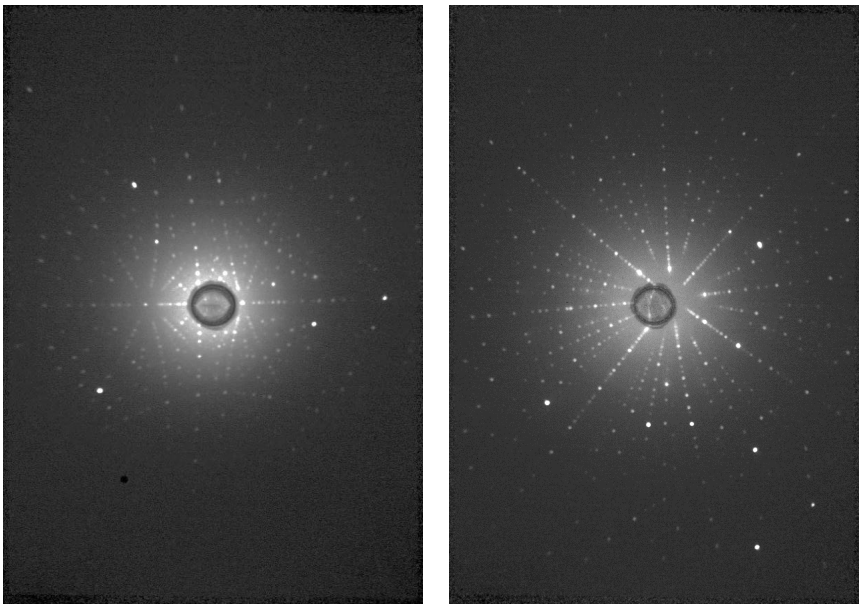

FIGURE 2.8: (LH): Laue diffraction pattern of the (100) direction (A-needle). (RH): Laue diffraction pattern taken from LSCO single crystal of the (001) direction (C-needle.)

2.4 SQUID Magnetometer

Superconducting Quantum Interference Devices (SQUIDs) are commonly used to detect the smallest magnetic signals and function as the on of most sensitive magnetic flux-to-voltage transducers. The SQUID relies on the physical principal of the Josephson junction making it sensitive to a change in magnetic flux of one flux quantum:

$$\Phi_0 = \frac{h}{2e} = 2.07 \times 10^{-7} G - cm^2 \tag{2.3}$$

The measurement system that was used in this work was a S600 SQUID SUSCEPTOMETER of CRYOGENIC LTD. This system can work either at a high a field regime up to 6.5 T, or at a low field regime up to 200 G, with field resolution of 0.01G. Conceptually, the measurement is performed by moving a sample trough

a set of pickup coils. The pickup coils are a set of three coils configured as a second-order gradiometer. In this configuration, the upper coil is a single turn wound clockwise, the center coil has two turns wound counter-clockwise and the bottom coil is again one turn wound clock wise. This configuration reduces noise in the detection system caused by the external magnetic field. The movement induces a change of magnetic flux and creates screening currents that flow into the flux transformer. This flux change is detected by the SQUID device. The output voltage is converted to physical units of magnetic moment.

Magnetic susceptibility data was measured at temperatures ranging between 4 K to 45 K with external field strengths varying from $H = 0.5$ Oe to $H = 100$ Oe. Magnetization measurements were done on the A- and C-needle samples, as seen in fig 2.6, with several doping levels. The samples were placed into a cylindrical teflon sample holder inside the measurement capsule, which guaranteed good alignment with the external field during measurements as seen in fig. 2.9.

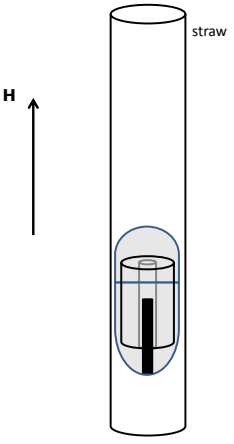

FIGURE 2.9: Measurement Configuration for SQUID experiment.

Prior to each measurement batch, the external field was calibrated with a Type I SC, to the actual zero field value of the magnet. Each measurement cycle began with heating the sample above T_c, slowly cooling it to 4 K at a rate of 1-2 K/min

in ZF, the field was then turned on and measurement were taken every 1K or 2 K at the plateaus, and every 0.05 K to 0.5 K on the superconducting transition.

Chapter 3

Results

In this chapter we will present our main experimental result and tests we performed verifying this result.

3.1 Main results

While measuring magnetization vs temperature on the LSCO crystals we noticed that there was a substantial difference between A- and C-needle samples, which were produced from the same crystal growth. In Fig. 3.1 we present the normalized magnetization as function of T (solid symbols). The measurement was done at a field of $H = 0.5$ Oe. Resistance data taken from the same section of the crystal that the needles were cut from is also shown (open symbols); ρ_{ab} is the in-plane resistance, and ρ_c is the resistance along the c-axis. Magnetization data in Fig. 3.1 exhibits clear difference of T_c between A and C needle samples. On the other hand, Resistance data exhibits no observable change in T_c between ρ_{ab} and ρ_c. The observed anisotropy of T_c for optimally doped LSCO was $\Delta T_c(15\%) = 0.65$ K, measured in the middle of the transiton. Since both sample are optimally doped, they lay on the flat region of T_c dome, small doping variation between samples, are not

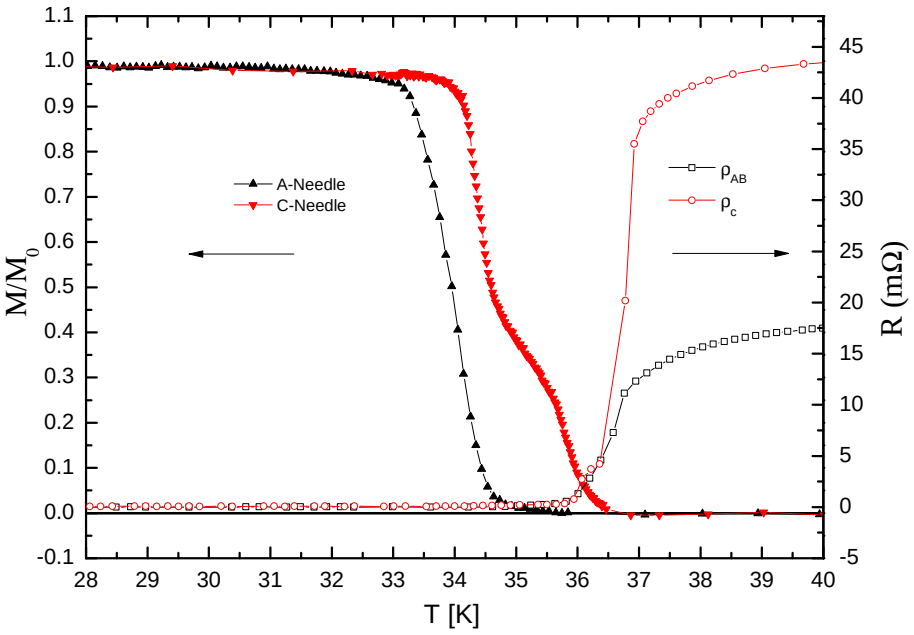

FIGURE 3.1: Anisotropy in T_c for optimally doped LSCO(x=0.15): Magnetization measured upon application of $H = 0.5$ Oe as a function of temperature. While the magnetization measurement has an apparent difference in T_c, while resistivity shows no difference between measurements.

likely to explain the discrepancy of T_c between samples. Figure 3.2 demonstrates results from a similar experiment preformed on sample with 7% and 8% doping. The 7% and 8% data exhibits even larger anisotropy between A- and C-needles of $\Delta T_c(7\%) = 4.5$ K and $\Delta T_c(8\%) = 2.6$ K respectivly. The larger anisotropy of the 7% samples suggests that this effect has doping dependence which will be later discussed in more details. We doubled checked these results, repeating the whole experiment on a separately grown crystals of both 7%, 8% and 15% doping, and witnessed the same behavior. The difference in T_c between the two directions is the main result of this work. Such a difference is not predicted by standard theories of superconductivity. It suggests that the transition to superconductivity in LSCO is a two dimensional one.

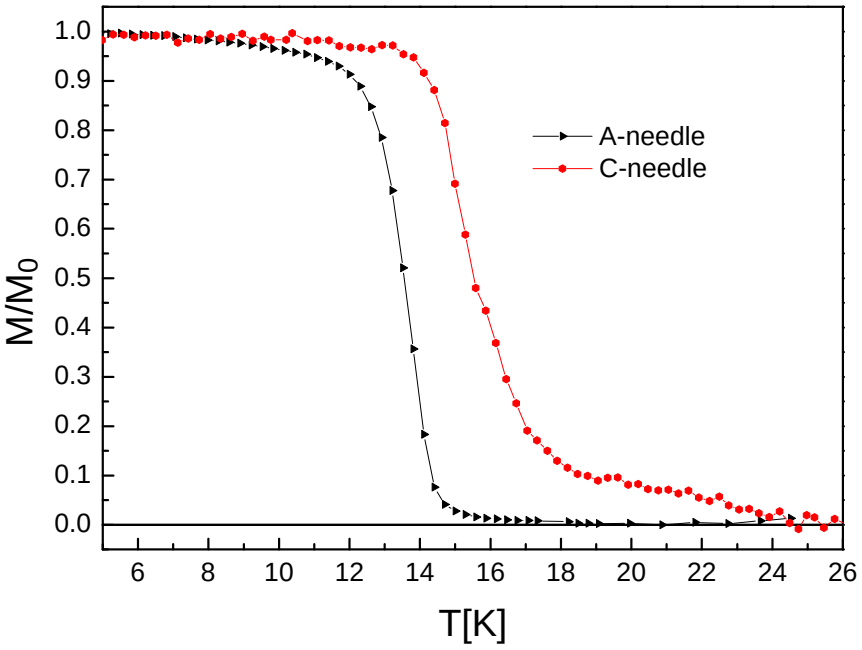

FIGURE 3.2: Anisotropy in T_c of LSCO with 8% Sr doping. Magnetization measured upon application of $H = 0.5$ Oe as a function of temperature.

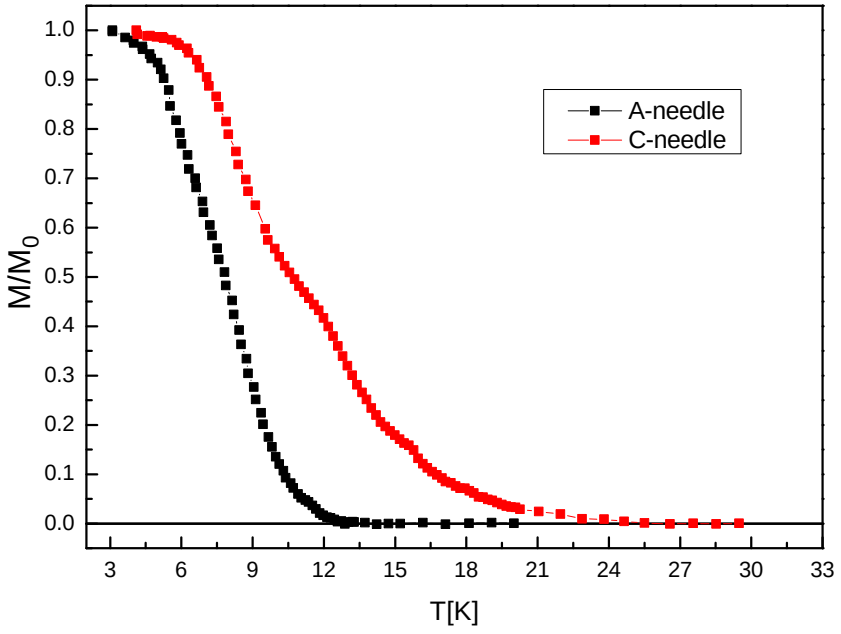

FIGURE 3.3: Anisotropy in T_c of LSCO with 8% Sr doping. Magnetization measured upon application of $H = 0.5$ Oe as a function of temperature.

3.2 Experimental Tests

3.2.1 Field Dependence and Volume Fraction

In order to verify these results we performed control experiments by changing one parameter at a time. In Fig. 3.4 and Fig. 3.5 we plot $4\pi\chi$ as a function of temperatures for several applied magnetic fields for the 15% samples using the A- and C-needles respectively.

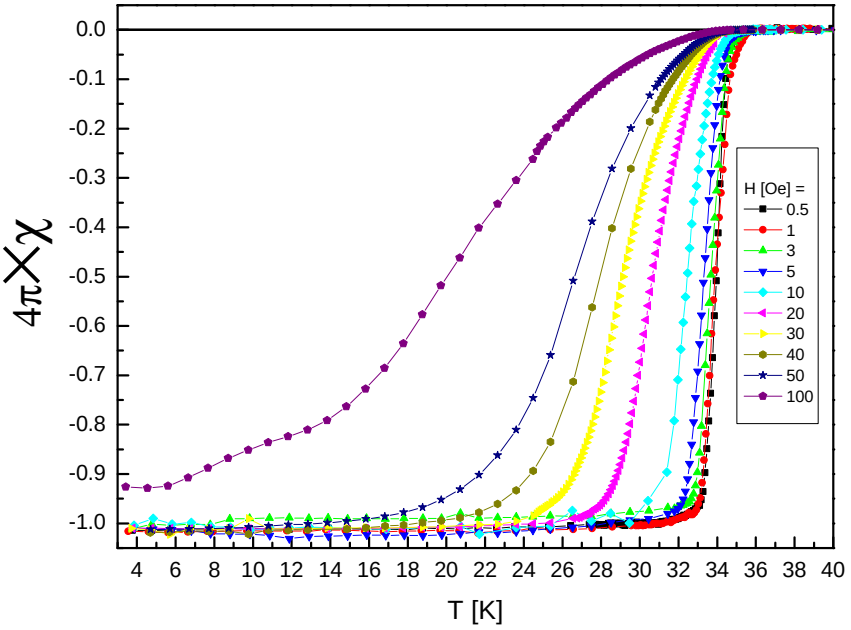

FIGURE 3.4: Magnetization as a function of T perpendicular (A-Needle) to c-axis in various magnetic fields

One can see that the saturation value of the susceptibility is field independent, this is more clearly visible in Fig. 3.7 where Magnetization as a function of T exhibiting linear behavior at the lowest temperature. Finally, as the field is lowered towards zero, the function $\chi(T)$ converges giving the zero field $\chi(T)$.

Both samples reached full SC volume fraction of $\frac{-1}{4\pi}$ after taking into account the demagnetization factor of a finite length needle like sample. For a rectangular

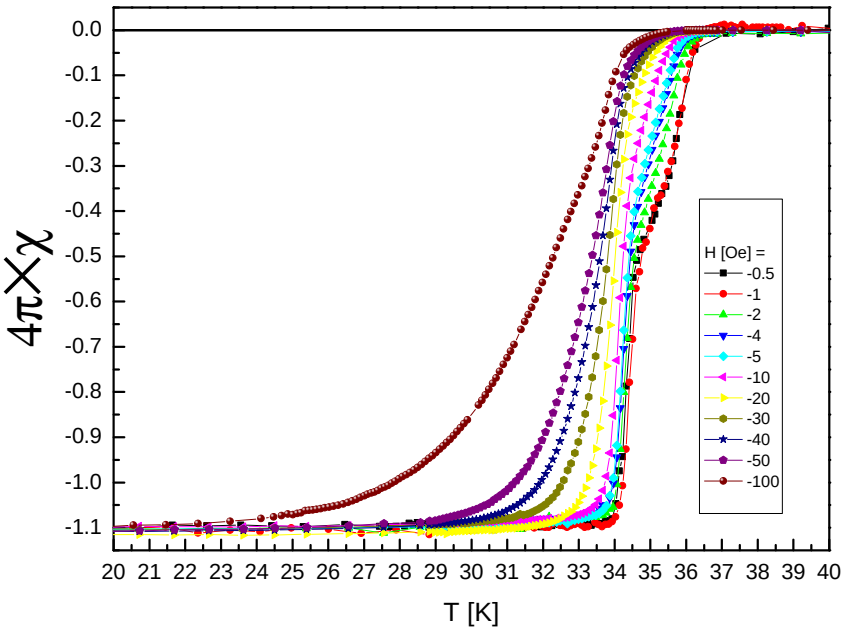

FIGURE 3.5: Magnetization as a function of T parallel (C-Needle) to c-axis in various magnetic fields

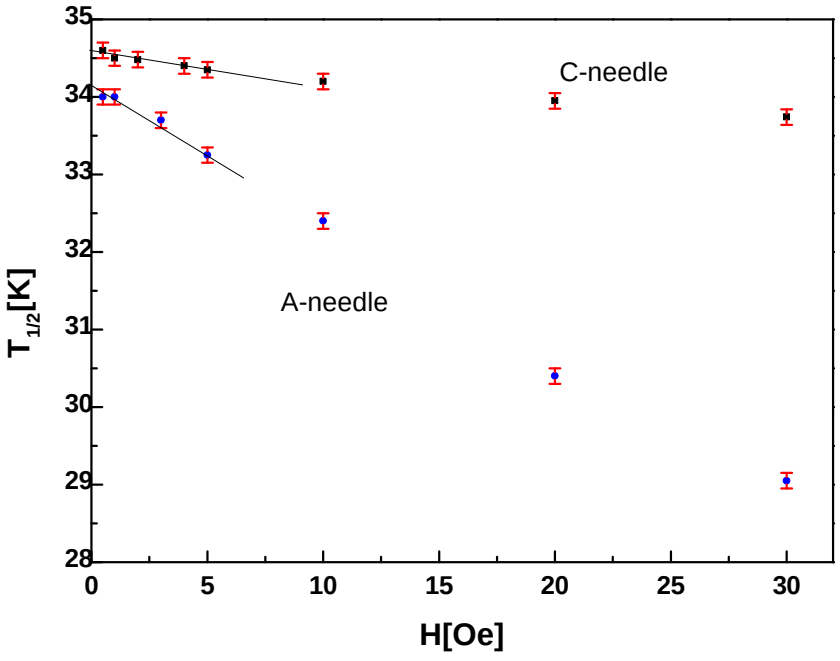

FIGURE 3.6: $T_{\frac{1}{2}}$ for parallel (C-needle) and perpendicular (A-needle) as a function of magnetic field for 15% $La_{1-x}Sr_xCuO_4$

A-needle sample with dimensions of $1 \times 1 \times 10$ with $l/d = 10$ as in our case $D \simeq 4\pi \times 0.045$. For a typical C-needle sample with dimensions of $1 \times 1 \times 5$ with $l/d = 5$ the demagnetization factor is $D \simeq 4\pi \times 0.09$. ([13])

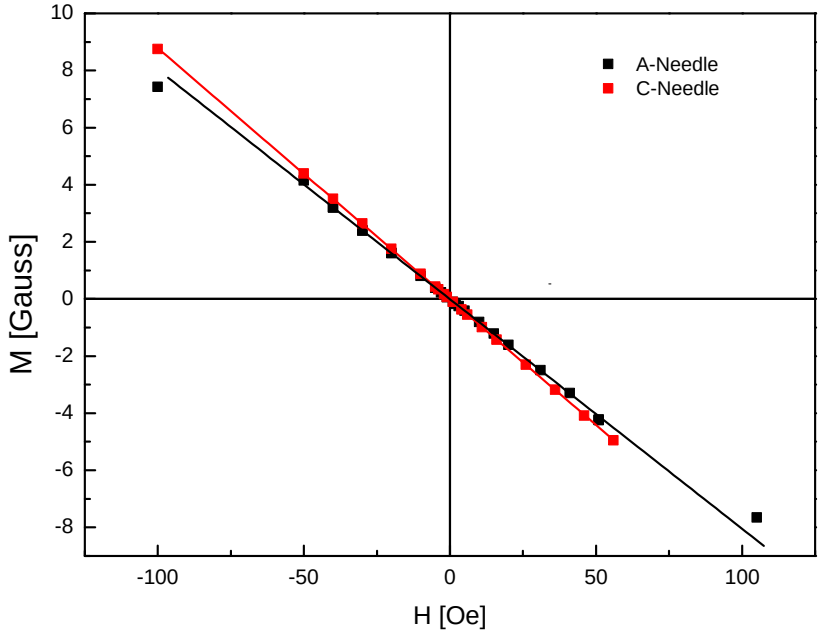

FIGURE 3.7: Magnetization as function of field for 15% doping A and C needle samples at $T = 4$ K

To see the field dependence of the transition more clearly, we defined a temperature, $T_{\frac{1}{2}}$, which corresponds to the T at which the susceptibility reaches one-half of it's initial value. Figure 3.6 clearly demonstrates the anisotropy of the slope at which $T_{\frac{1}{2}}$ decrease as a function of field between A and C needle samples. It also demonstrates that $T_{\frac{1}{2}}$ converges to a finite value when $H \to 0$, giving the zero field ΔT_c.

3.2.2 Critical Fields Temperature Dependence

One of our concerns with these results were vortices. If at a certain temperature, the H_{c1} value of the samples drops below the applied magnetic field, then we can no longer argue that we are working in the London limit where the field is finite only out of the sample and on it surface. While at low temperatures it is easy to resolve this matter, at higher temperature, close to T_c it is not that simple. Therefore, it was important to understand the behavior of H_{c1} near the superconducting transition. In order to accomplish this, we slowly cooled the A and C needle samples at ZF than gradually heated the sample to a desired temperature. At this temperature we swept the field up while taking magnetization measurements. The cooling-heating cycle was repeated before taking measurements by sweeping the field down. This was repeated for several temperatures near the superconducting transition. Figures 3.8 and 3.9 show the magnetization as a function of magnetic field for the A- and C- needle samples respectively. The values of H_{c1} were determined as the difference in the magnetic field between the peaks in the magnetization, at each measured temperature. These results clearly show that we are working in the London limit, up to temperatures at which the superconducting volume fraction drops to values smaller than 10%. In other words, until very close to T_c, our working field is smaller than H_{c1}.

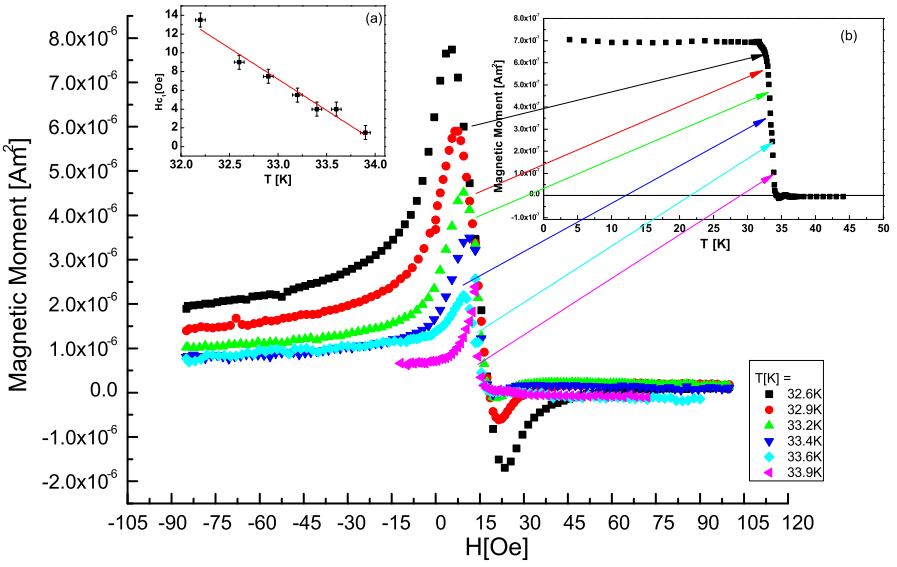

FIGURE 3.8: Main Graph: Magnetization as a function of magnetic field of the 15% A-needle in several temperatures along the superconducting transition. Insets: (a): H_{c1} as a function of temperature. (b): Magnetization as a function of T at $H = 0.5$ Oe demonstrating where measurements were taken.

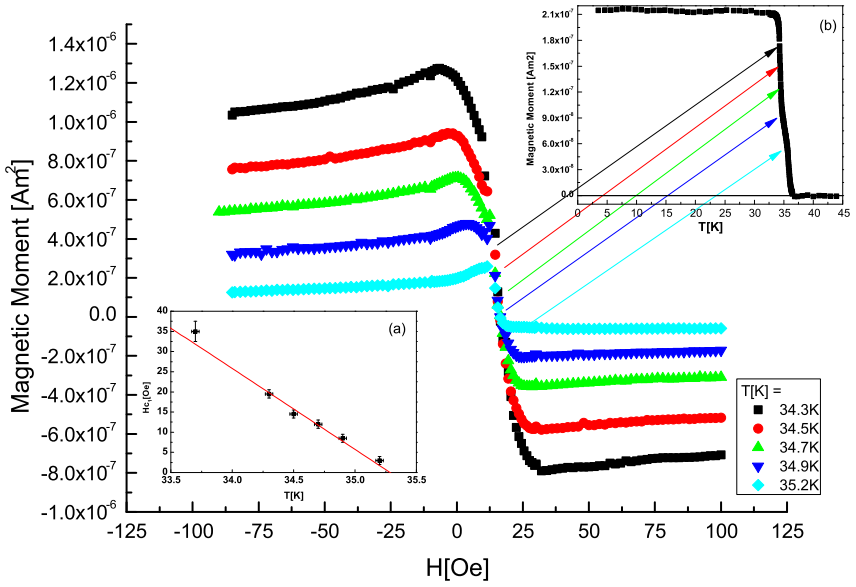

FIGURE 3.9: Main Graph: Magnetization as a function of magnetic field f the 15% C needle in several temperatures along the superconducting transition. Insets: (a): H_{c1} as a function of temperature. (b): Magnetization as a function of T at $H = 0.5$ Oe demonstrating where measurements were taken.

3.2.3 Sample Homogeneity

Another factor that could undermine our results is the possibility of big Sr doping x variation along the grown crystals. In order to test this claim, we sliced a crystal of LSCO with 8% doping into ten thin disks. Figure 3.10 presents the T_c's of these disks, measured by squid, as a function of position from the point where a single grain starts forming in the growth. The measured fluctuation in T_c along the rod was found to be 0.25 K, while the ΔT_c between the 8% A- and C-needles was 2.6 K. This means that doping variation by itself, cannot explain the results we see. Moreover, previous works performed using wavelength dispersion spectroscopy (WDS) have shown that in $La_{1-x}Sr_xCuO_4$ crystals, the Sr content stabilizes at its nominal concentration after roughly 10 mm of growth [14]. We cut our samples at longer distance which ensure almost uniform Sr content of our sample.

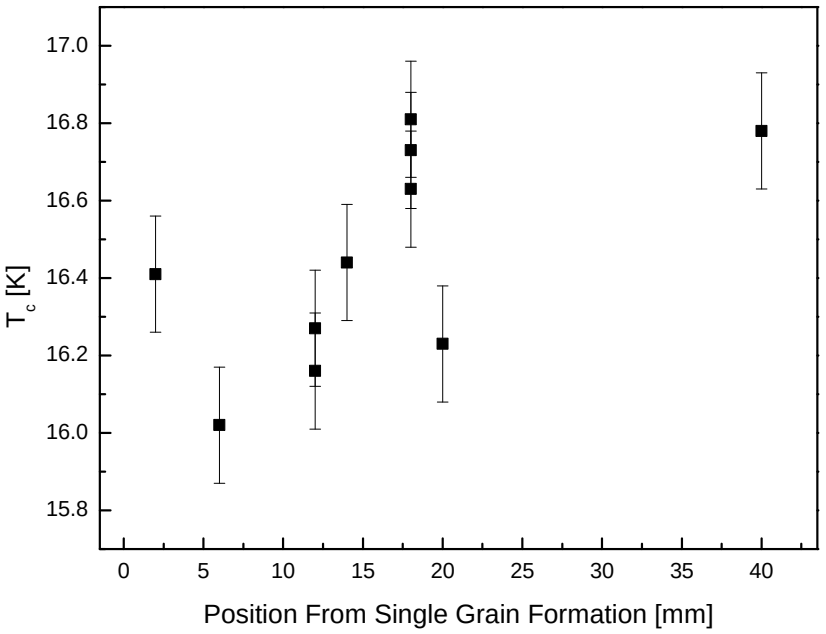

FIGURE 3.10: Sr homogeneity along the grown crystal via T_c in 8% LSCO

3.2.4 Geometry Dependence

Due to the possibility that miss-orientated and sample length can influence the data, we changed the sample and the measurement geometry to further verify our findings. We intentionally tilted a 15% *A*-needle sample with a sample holder described in chapter 2, only with a diagonally drilled insert, producing roughly 7 degrees misalignment angle. Figure 3.11 shows two magnetization curves, one with the normal and the second with a tilted sample. The difference between the two measurements is small. Thus low angle miss-orientation cannot account for our measured ΔT_c. The same measurements were repeated on a *C*-needle sample, with no significant difference observed between them.

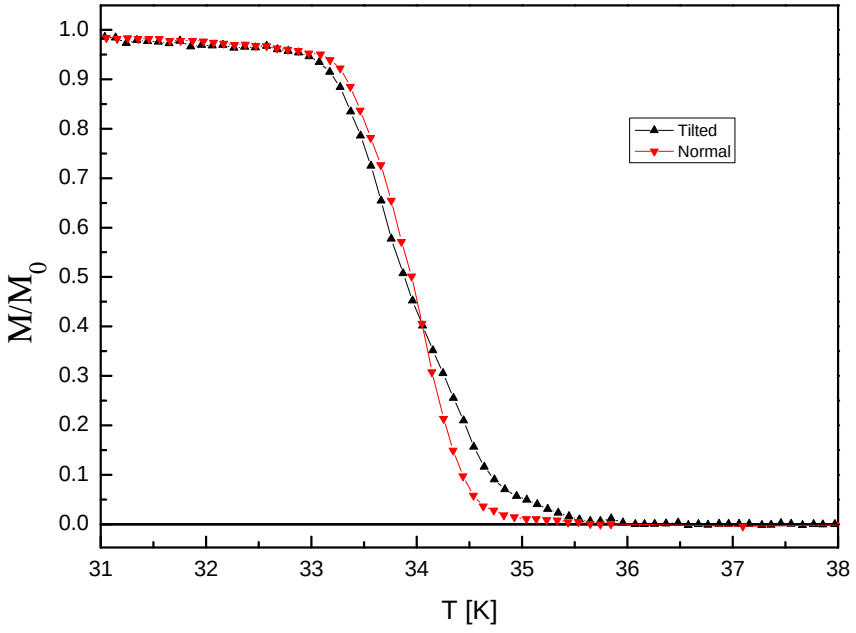

FIGURE 3.11: A Comparison between a 15% A needle sample tilted by 7 degrees of axis and a non tilted sample.

Figure 3.12 shows a comparison between two sample lengths, the 10 mm needle and a 5 mm needle which was cut out of the original 10 mm needle. It is clear that there is no significant difference between the two measurements, indicating

that our results are not sensitive to the sample's length if the needle shape is maintained.

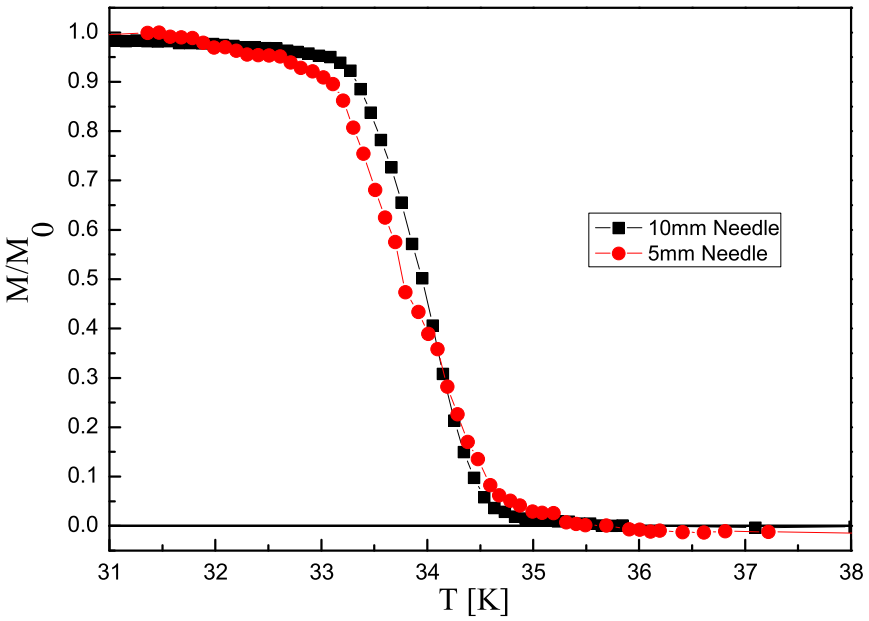

FIGURE 3.12: Comparison between a 10 mm and 5 mm 15% A needle samples. The 5mm needle was cut from the original 10 mm sample.

All of the testes reported above support our observations that there is an anisotropy in the intrinsic susceptibility of LSCO and that the critical temperatures of an *A*- and *C*-needle are different by an amount bigger than any possible experimental error. In addition, we cut out a cube shaped sample out of the 7% crystal with $4\times4\times3$ mm dimensions, with the *c*-axis pointing along the 3 mm face. Figure 3.13 shows both measurements for two orientation, with $H \parallel$ to the *c*-axis and $H \parallel$ to the *ab*-planes. The anisotropy between the two direction is clearly visible here, by either extrapolation, or simply by looking for the temperature at which the signal becomes paramagnetic (inset). We would also like to point out that this data was measure on the SAME sample, which by itself emphasizing the fact that the anisotropy is intrinsic. This measurement also underlines the importance of sample geometry when measuring orientation dependent susceptibility. When measuring

magnetization of cube or sphere shaped samples, what is actually measured is a mix of the two susceptibilities.

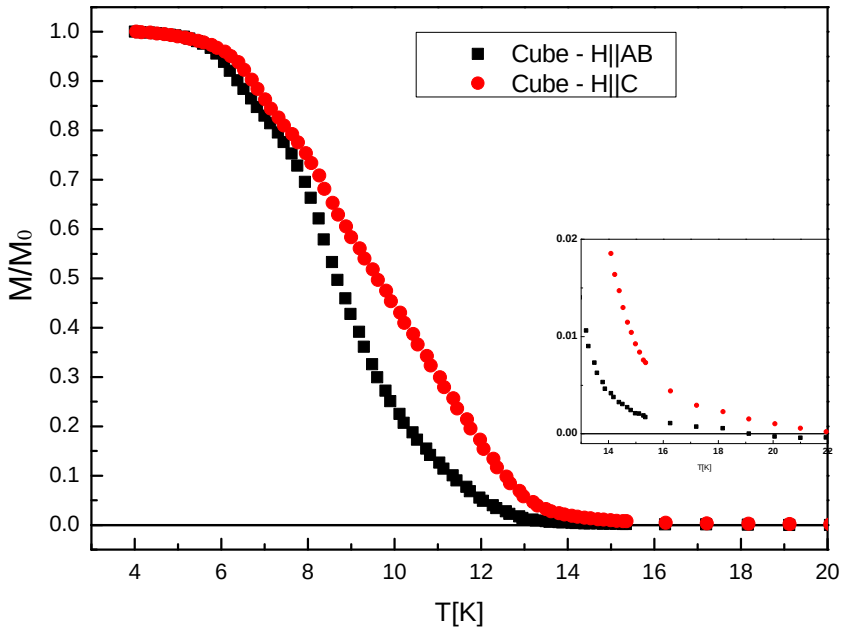

FIGURE 3.13: Magnetization vs T measure on a 7% cube shaped sample for two orientations. Inset: Zoom-in to the onset of the SC transition

Chapter 4

Discussion

In this chapter we will discuss the experimental result and try to connect between theory and experiment.

4.1 The Anisotropic London Equation

Our measurement revealed anisotropic susceptibility between the two measured directions. The most significant difference was expressed in what seems to be a T_c variation between the two directions. This difference leads us to think that we are witnessing a two-dimensional phase transition with long range order. Since this is theoretically impossible one might explain the T_c variation as a finite size effect, namely, there is only one T_c but the penetration depth diverges at a different rate vs T for the two different measurement directions. As a consequence, the penetration depth is on the scale of the sample size at different temperatures for the two different direction. From a practical point of view our magnetometer picks-us a diamagnetic signal only when the penetration depth is shorter than the sample size. Therefore, different diverging rates behaviour of the penetration

depth might lead to an erroneous interpretation of the data as having two different T_c in two different measurement directions.

Therefore, we would like to examine better the London penetration depth (λ). Since the measurements were performed on rectangular needles, we can assume that the magnetic field penetrates the samples in the following manner (Fig. 4.1): for the C-needle samples, the field penetrate the sample only with the penetration depth λ_{ab} but in the A-needles samples, the field penetrates through both λ_{ab} and λ_c. This assumption is only valid as long as we work in the London limit, namely, the applied field H is below the critical magnetic field H_{c1}.

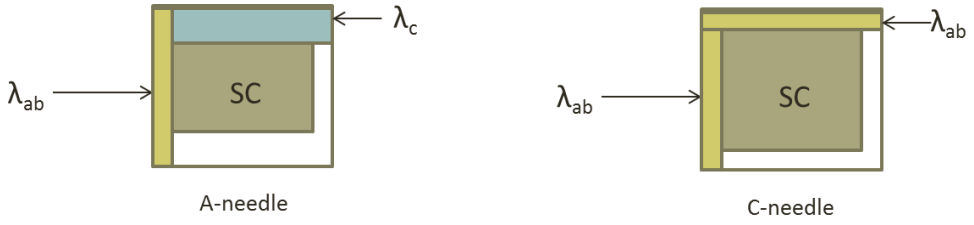

FIGURE 4.1: Schematic draw of the magnetic field penetration into the A and C needle samples.

In what follows we derive the London equation for an anisotropic superconductor. We use **b** as the microscopic field, and **J** as the total current (not just the external one). We define $\mathbf{B} = \langle \mathbf{b} \rangle$ as the average over a cross section of the sample. Since **J** is the total current there is no difference between magnetic induction **B** and magnetic field **H**. The London equation for isotropic penetration depth is,

$$\mathbf{J} = -\frac{e^2 n_s}{mc}\mathbf{A}. \tag{4.1}$$

This can be written as,

$$\mathbf{A} = -\frac{mc}{e^2 n_s}\mathbf{J}. \tag{4.2}$$

For anisotropic penetration depth, in a 2D geometry ($J_z = 0$), this changes into,

$$\mathbf{A} = -\frac{c}{e^2 n_s}\left(m_x J_x \widehat{\mathbf{x}} + m_y J_y \widehat{\mathbf{y}}\right) \tag{4.3}$$

Taking the rotor of both sides gives,

$$\mathbf{b} = b\widehat{\mathbf{z}} = \nabla \times \mathbf{A} = \frac{-c}{e^2 n}\left(m_y \frac{\partial J_y}{\partial x} - m_x \frac{\partial J_x}{\partial y}\right)\widehat{\mathbf{z}} \tag{4.4}$$

The Maxwell equation is,

$$\nabla \times \mathbf{b} = \frac{4\pi}{c}\mathbf{J} \tag{4.5}$$

Since $\mathbf{b} = b\widehat{\mathbf{z}}$,it means that,

$$J_x = \frac{c}{4\pi}\frac{\partial b}{\partial y} \tag{4.6}$$

and,

$$J_y = -\frac{c}{4\pi}\frac{\partial b}{\partial x}. \tag{4.7}$$

Therefore

$$b = \frac{c^2}{4\pi e^2 n}\left(m_y \frac{\partial^2 b}{\partial x^2} + m_x \frac{\partial^2 b}{\partial y^2}\right) \tag{4.8}$$

or,

$$b = \lambda_x^2 \frac{\partial^2 b}{\partial x^2} + \lambda_y^2 \frac{\partial^2 b}{\partial y^2} \tag{4.9}$$

with,

$$\lambda_x^2 = \frac{c^2 m_y}{4\pi e^2 n} \tag{4.10}$$

and,

$$\lambda_y^2 = \frac{c^2 m_x}{4\pi e^2 n}. \tag{4.11}$$

Another way to reach eq. 4.9 is given in Appendix B.

One has to solve the differential equation under the assumption that outside the sample some external field b_{ext} is given. It is convenient to divide eq.4.9 by b_{ext}

and to rename $b/b_{ext} \rightarrow b$ but now the condition is that outside of the sample $b = 1$. Once the equation is solve we calculate

$$B = \langle b \rangle = \frac{1}{a^2} \int b(x, y) \cdot d\mathbf{a}. \tag{4.12}$$

If the sample is small compared to the dimensions of the squid pickup loop one can show that the signal divided by the applied field χ is given by

$$\chi = (B - 1)/4\pi. \tag{4.13}$$

Using equation 4.9, we can now relate the measured susceptibility to the penetration depth for each direction. The equations to be solved for obtaining λ_{ab} and λ_c are

$$\chi_a - \lambda_{ab}^2 \frac{\partial^2 \chi_a}{\partial^2 x} - \lambda_c^2 \frac{\partial^2 \chi_a}{\partial^2 y} = 0 \tag{4.14}$$

$$\chi_c - \lambda_{ab}^2 \frac{\partial^2 \chi_c}{\partial^2 x} - \lambda_{ab}^2 \frac{\partial^2 \chi_c}{\partial^2 y} = 0 \tag{4.15}$$

$$\tag{4.16}$$

χ_a and χ_c are susceptibilities of the A- and C-needle samples respectively (figure 4.1). The solution of these two equations provides $\chi_c(\lambda_{ab})$ and $\chi_a(\lambda_{ab}, \lambda_c)$ one can obtain λ_{ab} equating the analytical solution to the measured susceptibility of the C-needle sample. Then substitute λ_{ab} into χ_a and extracting λ_c by comparing the analytical solution to susceptibility of the A-needle sample.

Figure 4.2 shows the calculated temperature dependence of both λ_{ab} and λ_c as a function of T calculated from the 7% doped LSCO susceptibility data (Fig.3.3). Two arrows show the temperature where H_{c1} is on the order of our measurement field (0.5 Oe). Furthermore, the measured H_{c1} for these samples reaches the zero at the same T as λ reaches the sample size, hence the notion of vortices is not

valid in our case. Therefore we can claim to be working in the London limit at any given T. One can also see that the apparent T_c occurs when the penetration depth reaches the sample's dimensions. Also, λ_{ab} and λ_c run away from each other as the sample is warmed towards T_c. This means that if we increase the thickness of our samples, we should expect larger anisotropy in the measured values of T_c. Moreover, in fig. 4.3 we plot the penetration depths on a log-log scale as a function of $(T_c - T)$. T_c was chosen as the onset T from the magnetization. We show that close to T_c the penetration depth exhibits the typical power law behavior where $\lambda \propto |T_c - T|^{-\gamma}$, with $\gamma_{ab} = 0.42 \pm 0.01$ and $\gamma_{ab} = 1.21 \pm 0.05$. This means that the two different penetration depths diverge with different T_c. In other words, our observation of different T_c in different directions contradicts the finite size scenario.

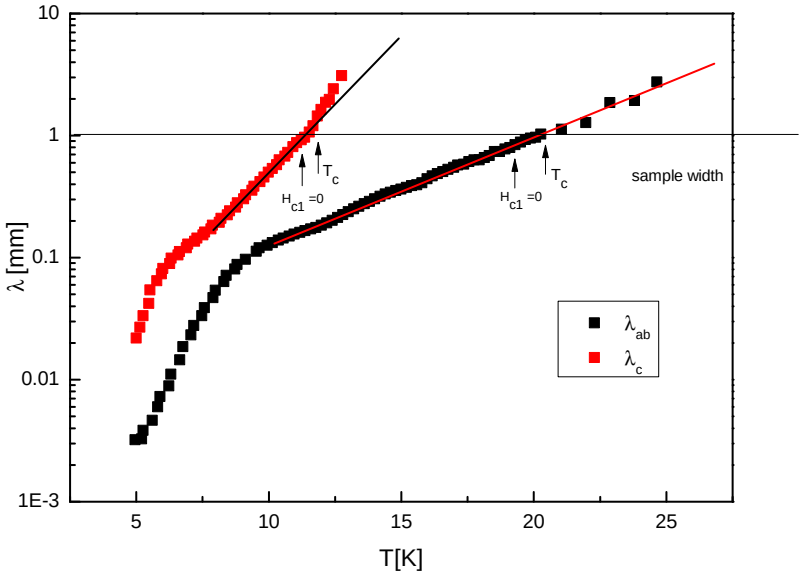

FIGURE 4.2: Penetration depth λ_{ab} and λ_c as a function of T for 7% doping plotted on a logarithmic scale.

From the extracted penetration depths we can also calculate the superfluid stiffness for each direction. In figure 4.4 we plot $\frac{1}{\lambda^2}$ as a function of T on a logarithmic scale. One can see that the in-plane superfluid density, ρ^s_{ab}, rises faster with decreasing

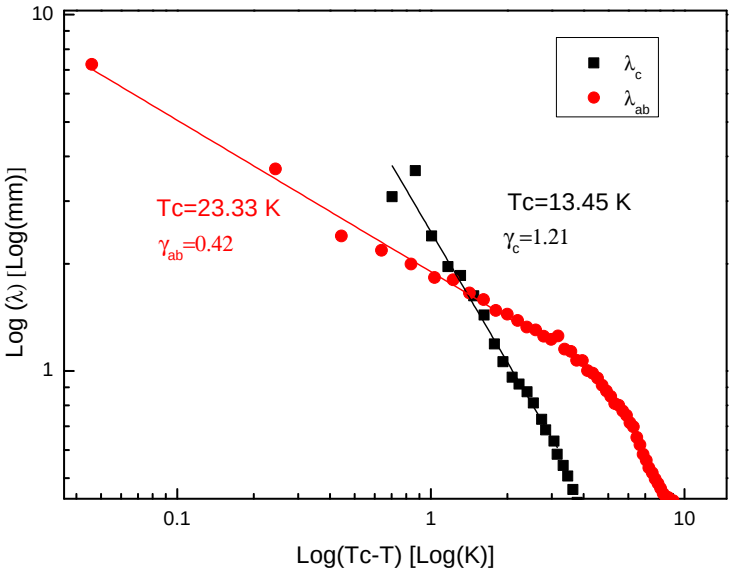

FIGURE 4.3: Penetration depths, λ_{ab} and λ_c, as a function of $(T_c - T)$ plotted on a log-log scale. T_c was chosen as the onset T from the magnetization.

T than the out-of-plane, ρ_c^s. This means that a certain temperature range the Cu-O planes are superconducting with no coupling between them. It is yet another indication of a 2D superconductivity.

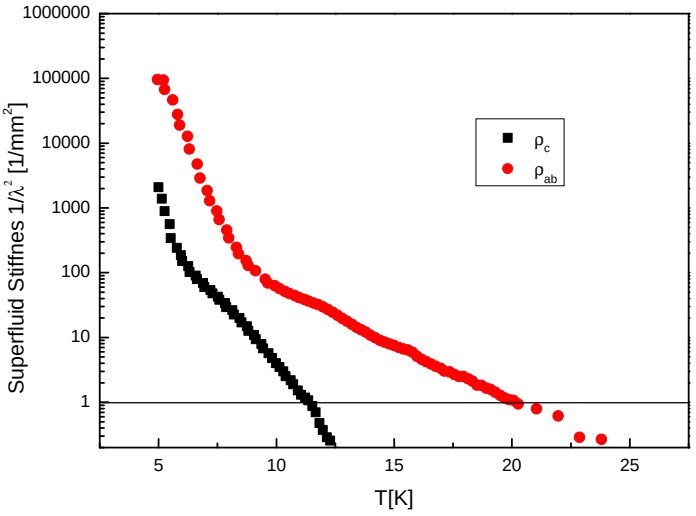

FIGURE 4.4: Measured Superfluid density (ρ^s) as a function of T for 7% doping. We consider $1[\frac{1}{mm^2}]$ as the value at which the superfluid stiffness vanishes.

If we turn now to Fig. 4.5, we can see the calculation done by Pekker[5] for the superfluid response (stiffness) vs T for a system which consists of layers with disorder in the c-axis direction. If we compare our calculated superfluid stiffness, ρ^s_{ab} and ρ^s_c, we notice a similar behavior in which ρ^s_{ab} rises at a higher T than ρ^s_c. In summary we can say that our result is in agreement with the theoretical prediction of two-dimensional phase transitions.

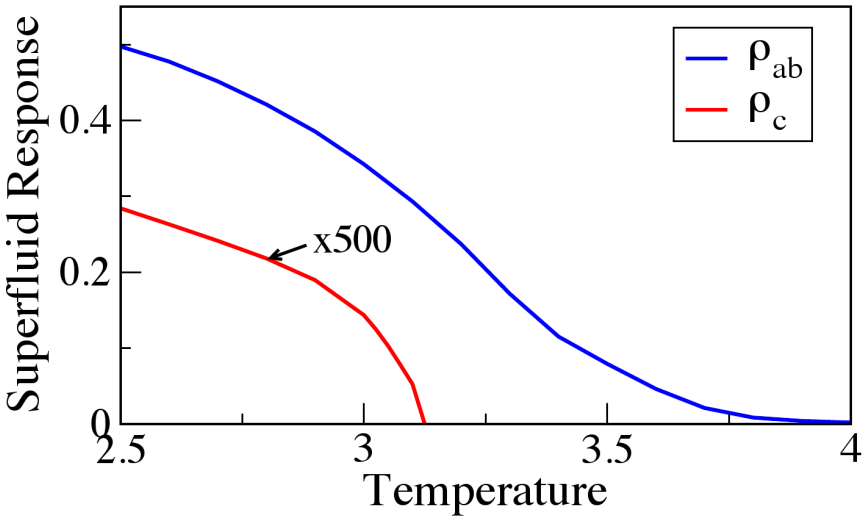

FIGURE 4.5: calculated in-plane (ρ^s_{ab}) and out-of-plane (ρ^s_c) superfluid response (stiffness) as a function of **simulation** T. adapted from in [5]

4.2 The Doping dependence of the 2D SC phase

In this work we measured samples of LSCO at various doping values, $x = 0.07$, 0.08, 0.12, 0.15. We found correlations between anisotropy of T_c and the doping level of our samples. As the Sr doping of the samples increases, ΔT_c between the AB- and C- directions decreases with a non linearly (fig. 4.6). For this purpose we define T_c in the most modest method, as the intersection between the linear part of the transition and the temperature axis.

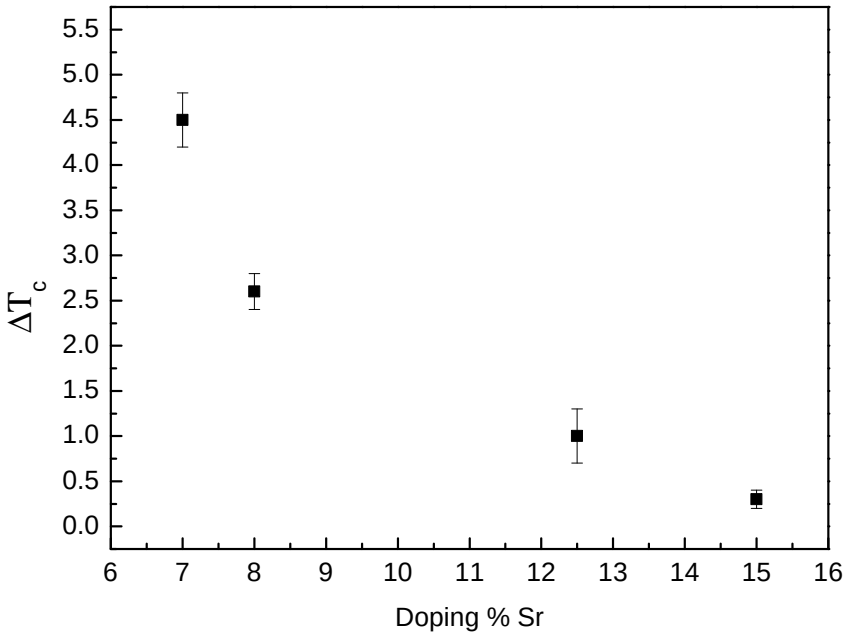

FIGURE 4.6: ΔT_c vs the doping of the LSCO samples. As the Sr doping increases, ΔT_c decreases non linearly.

The correlation between ΔT_c and doping level can be explained by the reduction of the Josephson-like coupling strength between neighboring planes [15], emphasizing the fact the we in fact observe de-coupling between the CuO planes in our samples.

Chapter 5

Conclusions

In this work we preformed magnetization measurements of high quality signal crystals of LSCO, which were oriented and cut into samples shaped as rectangular needles with two different orientations.

We found anisotropic behavior of the SC transition temperature between different measurement directions at very low fields. Contrary to theoretical considerations, the data presented in this work indicates that there is a temperature region at which $La_{2-x}Sr_xCuO_4$ exhibits two-dimensional SC from a Meissner Effect point of view. There is a small temperature range in which long range superconductivity exists in the ab plane, but no long range superconductivity exists betweens planes. This can be interpreted as due-to two-dimensional superconductivity. We repeated the measurements on a series of samples with various doping and confirmed these results. Moreover, the anisotropy in T_c was found to have a strong doping dependency; it increased in the underdoped samples. We have performed a series of tests which have shown that this anisotropic behavior cannot be attributed to external factors, and is in fact an intrinsic phenomena. Moreover, we were able to extract the London penetration depths for both directions and to calculate the

superfluid stiffness. We demonstrated that the observed T_c variation is not a finite size effect. Despite our surprising result, we found and presented recently published experimental and theoretical works supporting it's possible existence.

Appendix A

The Demagnetization Factor

We will look at the simple case where a sample is not magnetized by itself, but can be magnetized upon application of an external magnetic field H. We will further assume that as a result of the external field the material developed a magnetization M in the same direction. Therefore the inner magnetic field is,

$$H_{in}^{total} = H - DM \tag{A.1}$$

D is known as the demagnetization factor and has different values depending on the geometry. The magnetic susceptibility χ_0 is defined as the ratio between the magnetization, M, and the total applied inner sample field H_{in}^{total}. For small enough applied fields, the magnetization will behave linearly as a function of field. The idea is that a particular moment does no know the origin of H and responds to the field H it experiences. Therefore,

$$M = \chi_0 H_{in}^{total} = \chi_0(H - DM) \tag{A.2}$$

Re writing the expression we get

$$M = \frac{\chi_0}{1 + D\chi_0} H \tag{A.3}$$

thus

$$\chi_m = \frac{\chi_0}{1 + D\chi_0} \tag{A.4}$$

Therefore, the measured susceptibility is different from the intrinsic one, and strongly depends on the geometry of the sample, for example a sphere has $D = \frac{4\pi}{3}$ while for an infinite needle, $D = 0$. We are interested in measuring the "clean" in and out-of-plane susceptibility, therefore we chose needle like sample which reduce D to minimum.

Appendix B

An Alternative Approach for the Anisotropic London Equation

An alternative approach for deriving the anisotropic London equation (proposed by Jorge Berger) is to express the free energy as,

$$F = \int \left[b^2 + \left(\lambda_x \frac{\partial b}{\partial x} \right)^2 + \left(\lambda_y \frac{\partial b}{\partial x} \right)^2 \right] dxdy \tag{B.1}$$

The variations is

$$b \rightarrow b + \delta b \tag{B.2}$$

$$F = \int \left[(b+\delta h)^2 + \left(\lambda_x \frac{\partial (b+\delta b)}{\partial x} \right)^2 + \left(\lambda_y \frac{\partial (b+\delta b)}{\partial x} \right)^2 \right] dxdy \tag{B.3}$$

$$F = \int \left[b^2 + 2b\delta b + \lambda_x^2 \left(\frac{\partial b}{\partial x}\frac{\partial b}{\partial x} + 2\frac{\partial b}{\partial x}\frac{\partial \delta b}{\partial x} \right) + \lambda_x^2 \left(\frac{\partial b}{\partial y}\frac{\partial b}{\partial y} + 2\frac{\partial b}{\partial y}\frac{\partial \delta b}{\partial y} \right) \right] dxdy \tag{B.4}$$

$$\delta F = 2 \int \left[b\delta b + \lambda_x^2 \left(\frac{\partial b}{\partial x}\frac{\partial \delta b}{\partial x} \right) + \lambda_x^2 \left(\frac{\partial b}{\partial y}\frac{\partial \delta b}{\partial y} \right) \right] dxdy \tag{B.5}$$

Integration by parts

$$\delta F = 2\int \left[b - \lambda_x^2 \frac{\partial^2 b}{\partial x^2} - \lambda_x^2 \frac{\partial^2 b}{\partial y^2} \right] \delta b dx dy + \left[\lambda_x^2 \frac{\partial b}{\partial x} \delta b \right]_{boundary} + \left[\lambda_y^2 \frac{\partial b}{\partial y} \delta b \right]_{boundary} \tag{B.6}$$

On the boundary $\delta b = 0$ so

$$\delta F = 2\int \left[b - \lambda_x^2 \frac{\partial^2 b}{\partial x^2} - \lambda_x^2 \frac{\partial^2 b}{\partial y^2} \right] \delta h dx dy \tag{B.7}$$

or

$$b - \lambda_x^2 \frac{\partial^2 b}{\partial x^2} - \lambda_x^2 \frac{\partial^2 b}{\partial y^2} = 0. \tag{B.8}$$

Both methods lead to the same equation. When used for needles we have for C-needle

$$b - \lambda_{ab}^2 \frac{\partial^2 b}{\partial x^2} - \lambda_{ab}^2 \frac{\partial^2 b}{\partial y^2} = 0, \tag{B.9}$$

and for A-needle

$$b - \lambda_c^2 \frac{\partial^2 b}{\partial x^2} - \lambda_{ab}^2 \frac{\partial^2 b}{\partial y^2} = 0. \tag{B.10}$$

Bibliography

[1] Q. Li, M. Hucker, G. D. Gu, A. M. Tsvelik, and J. M. Tranquada. Two-dimensional superconducting fluctuations in stripe-ordered $La_{2-x}Sr_xCuO_4$. *Phys. Rev. Lett.*, 99(6):067001, 2007.

[2] A. A. Schafgans, A. D. LaForge, S. V. Dordevic, M. M. Qazilbash, W. J. Padilla, K. S. Burch, Z. Q. Li, Seiki Komiya, Yoichi Ando, and D. N. Basov. Towards a two-dimensional superconducting state of $La_{2-x}Sr_xCuO_4$ in a moderate external magnetic field. *Phys. Rev. Lett.*, 104(15):157002, 2010.

[3] J. M. Tranquada et al. Magnetic-field-induced uniaxial resistivity in a high-tc superconductor. *con-mat*, (arXiv:1009.0031v2), 2010.

[4] E. Berg, E. Fradkin, E.-A. Kim, S. A. Kivelson, V. Oganesyan, J. M. Tranquada, and S. C. Zhang. Dynamical layer decoupling in a stripe-ordered high-T_c superconductor. *Phys. Rev. Lett.*, 99(12):127003.

[5] David Pekker, Gil Refael, and Eugene Demler. Finding the elusive sliding phase in the superfluid-normal phase transition smeared by c-axis disorder. *Phys. Rev. Lett.*, 105(8):085302, 2010.

[6] Priyanka Mohan, Paul M. Goldbart, Rajesh Narayanan, John Toner, and Thomas Vojta. Anomalously elastic intermediate phase in randomly layered superfluids, superconductors, and planar magnets. *Phys. Rev. Lett.*, 105(8): 085301, 2010.

[7] J.G.Bednorz and K.A.Müller. Possible high T_c superconductivity in the Ba-Ba-Cu-O. *Z. Phys. B:Cond Mat*, 64, 1986.

[8] R. J. Cava et al. Bulk superconductivity at 91 k in single-phase oxygen-deficient perovskite $Ba_2YCu_3O_{9-\delta}$. *Phys. Rev. Lett.*, 58(16), 1987.

[9] L. Gao et al. Superconductivity up to 164 k in $HgBa_2Ca_{m-1}Cu_mO_{2m+2+\delta}$ (m=1, 2, and 3) under quasihydrostatic pressures. *Phys. Rev. B*, 50(6):4260–4263, 1994.

[10] Z. Hussain A. Damascelli and Z. Shen. *Rev. Mod. Phys.*, 75(2), 2003.

[11] J. Orenstein and A. J. Millis. Advances in the physics of high-temperature superconductivity. *Science*, 288(5465), 2000.

[12] E. Torikai K. Nagamine H. Kitazawa, K. Katsumata. Coexistence of magnetic ordering and superconductivity in La-Sr-Cu-O system revealed by positive muon spin relaxation. *Solid State Communications*, 67(12), 1988.

[13] M. Sato and Y. Ishii. Simple and approximate demangeritzation factors of uniformily magnetized rectengular rod and cylinder. *J. Appl. Phys.*, 66(2), 1982.

[14] Jiaqiang Yan. *A Study of bond-lenght flunction in transition metal oxides.* PhD thesis, The University of Texas at Austin, 2004.

[15] K. Kishio, J. Shimoyama, T. Kimura, Y. Kotaka, K. Kitazawa, K. Yamafuji, Q. Li, and M. Suenaga. Carrier doping and interlayer coupling in htsc single crystals. *Physica C: Superconductivity*, 235-240(Part 4):2775 – 2776, 1994.

על מוליכות דו מימדית בגבישים יחידים של $La_{2-x}Sr_xCuO_4$

גיל דרצ׳וק

על מוליכות דו מימדית בגבישים יחידים של $La_{2-x}Sr_xCuO_4$

חיבור על מחקר

לשם מילוי חלקי של הדרישות לקבלת התואר מגיסטר
למדעים בפיסיקה

גיל דרצ'וק

הוגש לסנט הטכניון – מכון טכנולוגי לישראל

אדר ב' תשע"א חיפה מרץ 2011

החיבור על מחקר הנעשה בהנחיית פרופ׳ עמית קרן

בפקולטה לפיסיקה

הכרת תודה

אני מודה לפרופ׳ עמית קרן על הנחיה, התמיכה, הסבלנות והעידוד במשך תקופת עבודתי בקבצותו

תודה מיוחדת לגלינה בזליצקי על עזרת בהכנת הדגמים וחברתה הנעימה. כמו כן תודה למני שי על עזרתו והכוונתו בתחילת הדרך. תודה לטכנאים ד״ר לאוניד יומין ושמואל הוידה על עזרתם.

תודה לכל חברי לקבוצת הטמפ׳ הנמוכות על התקופה המהנה.

תודה מיוחדת ללינה על האהבה והסבלנות.

אני מודה לטכניון על התמיכה הכספית הנדיבה במשך

השתלמותי.

תקציר

בגלל המבנה השכבתי של מוליכי-העל ממשפחת הקופרטים, ניתן היה לחשוד כי תופעת מוליכות העל מתקיימת רק בתוך המישורי החמצן-נחושת הדו מימדיים, אלא שתאורמת מרמין-וואגנר מציינת שמעבר פאזה כזה אינו אפשרי. מעברי פאזה במערכות שבהן פרמטר הסדר הוא רציף, מחייבת שלושה מימדים ולכן איננו רואים מגנטים דו-מימדיים או עיבוי בוזה-איינשטיין בשני מימדים. במשך שנים הפרדיגמה הרווחת הניחה כי על-מוליכות מתקיימת גם כן רק בשלושה מימדים, כלומר קיימת טמפרטורה קריטית (T_c) שבה כל המישורים הופכים על-מוליכים עם פאזה אחידה של פרמטר הסדר העל-מוליך בכל המישורים. למרות זאת, מחקרים חדשים גילו כי מוליכות העל יכולה להתקיים גם כאשר הצימוד בין מישורי הנחושת חמצן מתנתק. בתרכובת ה-LBCO, בהפעלות שדות מגנטים בעוצמה של מספר טסלות, נמדדה התנגדות גבוהה מהרגיל מתחת לטמפרטורה הקריטית בניצב למישורים כאשר במקביל אליהם נמדדה התנגדות אפסית. עבודה נוספת בנושא הראתה שבהפעלת שדה מגנטי בניצב למישורים, ניתן לנתק הצימוד בין המישורים העל מוליכים אך לקבל מוליכות-על מלאה בתוכם.

בעקבות עבודות אלו הוצעו מספר תיאוריות אשר גורסות כי כאשר יש משחק בין העל-מוליכות לבין סידור פסים מרחבי בתוך המישור, נוצרת פרסטרציה של הפאזה של פרמטר הסדר העל-מוליך הגורמת לניתוק המישורים. השערות נוספות הטוענות כי במערכות הבנויות משכבות כגון מגנטים, מוליכי על קופרטים וכו, אי-סדר בציר הניצב לשכבות יוצר מצב שבו השכבות נפרדות ועוברות מעבר פאזה דו מימדי בטמפרטורה גבוהה מזו של מעבר הפאזה התלת-מימדי.

למרות העדויות הנסיוניות שנאספו במהלך השנים לתופעות של מוליכות-על דו-מימדית, הניסוים נערכו בשדות מגנטים גבוהים, דבר שעלול להשפיע על מצב היסוד של המערכת. בנוסף לכך, במדידות הולכה מספיק למצוא נתיב אחד חסר התנגדות על מנת למדוד מוליכות-על ולכן, סימן ההיכר האמיתי של מוליכות על הינו "אפקט מייסנר" בשדות מגנטים נמוכים מהשדה הקריטי של החומר - גבול לונדון.

בעבודה הנוכחית חקרנו את הממדיות של מעבר הפאזה העל-מוליך בגבישים יחידים של $La_{2-x}Sr_xCuO_4$ (LSCO) בעלי רמות סימום שונות, על ידי מדידות

מגנטיזציה תלויות כיוון בשדות מגנטים נמוכים. הסימום של החומר נעשה על ידי הוספה של סטרונציום (Sr) במקום הלאנטאנום (La). בדרך זו ניתן לשנות את ריכוז החורים נושאי המטען במישורי החמצן-נחושת ובכך להעביר את החומר ממצב של מבודד מוט למצב של מוליכות על, ובנוסף לשלוט על הטמפרטורה הקריטית.

את הגבישים היחידים גידלנו באמצעות טכניקת ה"אזור המותך הנע". בטכניקה זו משתמשים בתנור בתוכו ממוקמות ארבע מראות פרבוליות ובמרכזן מורכבות מנורות בעלות הספק גבוה. המראות מרכזות את האור אל מוט קרמי מהחומר אותו רוצים לגדל ויוצרות בו אזור נוזלי מותך אשר מועבר בקצב איטי לאורך כל המוט ומתוך הנוזל המותך המוצק מתגבש לגביש יחיד. לגבישים שגידלנו ביצענו אוריינטציה באמצעות מצלמת לאוה (Laue Camera), על מנת לקבוע את הצירים הקריסטלוגרפים שלהם. לאחר האוריינטרציה הגבישים נחתכו לדגמים בצורת מחטים בעלי שתי אוריינטציות שונות, אחת עם המישורים מקבילים לציר המחט (a-needle) והשניה בה המישורים ניצבים לציר המחט (c-needle). החיתוך נעשה באמצעות מסור חיתוך יהלום מיוחד בו משולבת יחידת הגוניומטר שמאפשר חיתוך לאחר האוריינטציה ללא שינויה. באמצעות קונפיגורצית מחטים זו אנחנו יכולים למדוד את התגובה המגנטית של מישורי הנחושת-חמצן ואת התגובה הניצבת להם, בצורה נקייה ללא "ערבוב" בין שני התרומות. כמו כן, שימוש בדגמים בצורת מחטים מקטין את השפעת הפקטור דמגנטיזציה, התלוי בצורה הגיאמטרית של הדגם, מכיוון שעבור מחטים ארוכות גודלו של פקטור זה קרוב מאוד לאפס.

את מדידות המגנטיזציה ביצענו במגנטומטר סקוויד (SQUID), אשר מאפשר לנו להגיע לרזולוציה גבוהה הן בשדה והן בטמפרטורה. המדידה מתבצעת על ידי תנועה של הדגם דרך סט סלילים הקולט את השינוי בשטף המגנטי ומעביר אותו אל יחידת הSQUID אשר ממירה את השינוי בשטף המגנטי למומנט מגנטי. הדגמים קוררו באופן איטי של 1-2 קלווין לשעה לפני כל מדידה, באפס שדה מגנטי חיצוני. לאחר תהליך זה הופעל שדה חיצוני קטן (0.5 אורסטד) ונמדדה המגנטיזציה של הדגמים.

הממצאים העיקריים בעבודה הנוכחית היו אניזוטרופיה משמעותית במגנטיזציה בדגמים שיוצרו מאותו גביש יחיד, בין שני כיווני המדידה (a- and c- needles) שהתבטאה בהבדל ב-T_c בין הדגמים. חזרנו על הניסוי עבור גבישים בעלי רמות סימום שונות של $x=0.07,0.08,0.12,0.15$, במהלכם הצלחנו לשחזר את התוצאה עבור כל הדגמים. בנוסף לכך, הבחנו כי ההבדל בT_c הופך משמעותי יותר ברמות

סימום נמוכות. ניתן להסביר זאת על ידי כך שהצימוד בין המישורים הולך ונחלש עם ירידת הסימום.

על מנת לאשרר את הממצאים שלנו, ביצענו סדרה של ניסוי בקרה על מנת לוודא כי האניזוטרופיה שנמדדה אינה נגרמת מגורמים חיצוניים. ביצענו מדידות עבור ערכים שונים של שדות חיוצוני, כדי לוודא כי אנו באמת עובדים בגבול לונדון ובפרט את הנפח העל מוליך של הדגמים. כדי להראות שאנו עובדים במערכת נטולת מערבולות מגנטיות, בחנו את התנהגות השדה הקריטי הראשון (H_{c1}) כתלות בטמפרטורה קרוב למעבר הפאזה. בדקנו והראנו כי הגבישים שגידלנו הם אכן הומוגנים ברמת הסימום שלהם לאורך כל הגידול. הראנו כי טעויות באוריינטצית הדגמים אינה גורמת להבדל משמעותי מספיק, וכמו כן בדקנו כציד משפיע גודל הדגמים על התוצאות. כל הבדיקות שביצענו הובילו אותנו למסקנה שהאניזוטרופיה בין הכיוונים היא תכונה פנימית ואינה תולדה של גורם חיצוני.

ההבדל ב-T_c שמדדנו בין שני הכיוונים הוביל אותנו לחשוב שמתרחש כאן מעבר פאזה דו-מימדי עם סדר ארוך טווח. מאחר ותיאורטית הדבר אינו אפשרי, ניתן היה להסביר את ההבדל ב-T_c כאפקט גודל-סופי הנגרם מכך שעומק החדירה בכיוונים השונים מתבדר בקצב שונה, כלומר, קיים רק T_c אחד. מאחר ואנו יכולים למדוד סיגנל מגנטי רק כאשר עומק החדירה קטן מגודל הדגם, קצב התבדרות שונה עלול בטעות להראות כ-T_c שונה בין שני הכיוונים. באמצעות משוואת לונדון הדו-מימדית חילצנו את עומקי החדירה בכיוונים השונים, והראנו שעומקי החדירה בכיוונים השונים מתבדרים עם T_c שונה. במילים אחרות, התוצאות שקיבלנו כאן מראות שההבדל ב-T_c אינו אפקט גודל-סופי. כמו כן, מתוך עומקי החדירה חישבנו את צפיפות נוזל העל מוליך לכיוונים השונים וראינו התאמה איכותית לחישובים תיאורטים. לסיכום, התוצאות שהוצגו בעבודה הנוכחית מצביעות על כך שב-LSCO מתרחש מעבר פאזה דו-מימדי עם סדר ארוך טווח ו-T_c שונות.

העבודה מסודרת כדלקמן:

- בפרק 1 אנו מסבירים את הרקע לעבודה שלנו ואת העבודות שנעשו בתחום.
- בפרק 2 מתאר את המערכות בהן השתמשנו להכנת הדגמים בניסוי. וכמו כן מוצגות את התיאוריות והעקרונות של שיטות המדידה בהן התשמשנו.
- בפרק 3 מובאות תוצאות הניסויים. ראשית מוצגות תוצאות ממדידות המגנטיזציה כתלות באוריינטצית הדגם, עבור סדרה של דגמים בעלי סימום שונה. לאחר מכן מוצגות תוצאות של ניסוי הבקרה בהן השתמשנו לוודא את התוצאות: מדידה בשדות מגנטים שונים, מדידת השדות הקריטים קרוב למעבר הפאזה, בדיקה של הומוגניות הסימום בגבישים שגידלנו ובחינת ההשפעה של גיאומטריית הדגמים על התוצאות.
- פרק 4 מציג דיון בתוצאות הניסוי ומקשר בין הניסיון לתיאוריה
- פרק 5 מסכם את העבודה שנעשתה במחקר זה.